Effects of aggregation kinetics on nanoscale colloidal solution inside a rotating channel

A thermal framework

Nilankush Acharya[1] · Kalidas Das[2] · Prabir Kumar Kundu[1]

Abstract

The objective of the present investigation is to reveal the effects of aggregation kinetics on the nanofluid flow between two revolving plates. Additionally, we have presumed that the upper surface of the revolving structure is permeable while the lower one is blessed to move with variable speed. Here we have introduced Nimonic 80A alloy nanoparticles with water as a base liquid. Aggregation kinetics at molecular level has been introduced mathematically to model our work and to explore how aggregation features affect the thermal integrity of the system. Similarity technique guided us to avail non-dimensional form of leading equations. RK-4 method along with shooting technique aids us to solve nonlinear ODEs. Several features of aggregation parameters on velocity and temperature profile have been explored through graphs and tables. Results extract that effective thermal conductivity of aggregated composite increases for nanoparticle volume fraction. Heat transport drops off for radius of gyration factor at lower segment but rises at upper regime.

Keywords Nanofluid · Nimonic 80A · Rotating channel · Aggregation kinetics · Heat transfer

Mathematics Subject Classification 76W05

List of symbols

Ω	Angular velocity
(u, v, w)	Velocity along x, y, z axis
U_w	Stretching velocity
T_0	Temperature of the upper surface
T_h	Temperature of the lower surface
T	Nanofluid temperature
ρ	Density
μ	Dynamic viscosity
κ	Thermal conductivity
(C_p)	Heat capacitance
v_w	Suction/injection parameter
$\alpha_\mathrm{nf} = \frac{\kappa_\mathrm{nf}}{(\rho C_\mathrm{p})_\mathrm{nf}}$	Nanofluid thermal diffusivity
ϕ	Nanoparticle volume fraction
ϕ_int	Nanoparticle volume fraction within aggregate
A_k	Kapitza radius
p	Aspect ratio
R	Average radius of gyration
d_f	Fractal dimension
d_l	Chemical dimension
N	Number of particles
a	Radius of primary particles
$\delta = \frac{bh^2}{v_\mathrm{f}}$	Reynolds number
$Pr = \frac{\mu_\mathrm{f}(\rho C_p)_\mathrm{f}}{\rho_\mathrm{f}\kappa_\mathrm{f}}$	Prandtl number
$S = \frac{v_\mathrm{w}}{bh}$	Suction/injection parameter
$\lambda = \frac{\Omega h^2}{v_\mathrm{f}}$	Rotation parameter
Nu	Nusselt number
C_f	Skin friction

✉ Nilankush Acharya
nilankushacharya@gmail.com

Kalidas Das
kd_kgec@rediffmail.com

Prabir Kumar Kundu
kunduprabir@yahoo.co.in

[1] Department of Mathematics, Jadavpur University, Kolkata, West Bengal 700032, India

[2] Department of Mathematics, Krishnagar Govt. College, Krishnagar, Nadia, West Bengal 741101, India

Nu_r	Reduced Nusselt number
C_{fr}	Reduced skin friction
$Re_x = \frac{U_w x}{v_f}$	Local Reynold's number

Subscripts

a	Aggregate
c	Backbone
nc	Dead end
f	Fluid
nf	Nanofluid
s	Nanoparticle
max	Maximum
eff	Effective

Introduction

Inferior thermal conductivity of usual fluid hinders elevated compactness and efficiency of heat exchangers. Hence, diverse amount of practice has been implemented to improve heat transfer. Enhancement of thermal features of energy transmission liquids may turn out to be a trick of expanding heat transfer. A groundbreaking approach of recuperating the thermal conductivity of usual liquids is to dissolve tiny metallic or non-metallic or polymeric particles, solid particles into fluids. Configuration of nanofluids includes particles with less than 100 nm diameter into conventional fluids. Dispersion of nanophase particles has most promising utility in heat transport including microelectronics, fuel cells or pharmaceutical equipments or hybrid-powered engines, nuclear reactor, cooling thermal behaviour in micro-vehicles, domestic refrigerator, chiller, heat exchanger, in grinding, machining and in boiler flue gas temperature reduction. Choi [1] bestowed the foremost contribution in designing and explaining the applicative features of nanofluid. Eastman et al. [2] experimentally explored that amplification in thermal conductivity about 60% can be gained for nanofluid consisting water plus 5% CuO nanoparticles. Implementation of nanofluids in solar system was depicted by Bozorgan and Shafahi [3]. Challenging features of TiO_2 nanofluids were illustrated by Yang and Hu [4]. Nanofoam for efficient microwave absorption is demonstrated by Li et al. [5]. Magnetite nanosuspensions with gifted phytotherapeutic features were reported in [6]. Heat transport function of CuO nanofluid was analysed by Manimaran et al. [7]. Impact of solar emission on bioconvective nanofluid flow in the presence of magnetic effect crossing over flat plate was investigated by Acharya et al. [8]. Akbar et al. [9] disclosed the heat transfer impression of magnetite nanofluid flow passing a stretched surface. Mixed convective flow of nanosolution inside a cavity along with slip mechanism and

inclined magnetic effect was explored by Ismael et al. [10]. MHD radiative graphene oxide with engine oil-based nanosuspension over porous stretched surface was addressed by Ghadikolaei et al. [11]. The outstanding literatures exploring the recent advancements on modelling- and simulation-based nanofluid flows have been addressed by Mahian et al. [12, 13]. They have communicated such benchmark presentation in two parts. The first part [12] involves application, thermophysical features and fabrication of nanofluids incorporating the molecular characters like Brownian motion, van der Waal force, thermophoresis, electrostatic forces, etc. They have theorized the topic for both single-phase modelling and two-phase modelling. Again in the second part [13], they have briefly summarized the leading computational techniques like finite difference, finite element scheme, lattice Boltzmann method, Lagrangian methods, etc. After that, various simulative works on 3D nanofluid flows over diverse configurations were deliberated. Difference between 3D and 2D simulations also holds a novel corner in this part.

Flow features and heat transport inside a channel are the significant phenomenon in thermal power generating coordination [14, 15], chemical reactors [16], gas turbines or nuclear plants, high temperature-based boiling plants [17], glass–fibre manufacturing [18, 19], or petroleum refineries as well as refrigeration process [20], heat exchangers [21, 22], turbo machinery. Core principle of such procedure is to diminish the drag effect and promotes heat transport. Fluid runs over rotating apparatus are framed by rotating frame of references. The energy transmitted among nanoliquid and rotor is noteworthy aspect in numerous rotating machines. Therefore, the investigations of revolving nanofluid flows will discover the opportunity of promoting heat transfer. Three-dimensional squeezed nanofluid inside spinning channel with the consideration of stretchable lower porous surface was reported by Freidoonimehr et al. [23]. Mohyud-Din et al. [24] addressed the heat–mass transport analysis of nanofluid inside spinning plates. Heat and stream investigation for magnetized nanosuspension under revolving system was discussed by Sheikholeslami et al. [25]. Mabood et al. [26] depict hydromagnetic variable viscous nanostream inside spinning permeable surfaces. Consequence of slip mechanism of iron nanoparticles among revolving stretched disc was elaborated by Hayat et al. [27]. Mustafa [28] illustrated the activities of spinning nanofluid stream. Control of active passive strategy of nanoparticles over revolving sphere was communicated by Acharya et al. [29]. Revolving MHD features of CNTs over stretched surface was communicated by Acharya et al. [30].

Alloys are generally composition of metal or metal plus another element. It has numerous applications aerospace system, nuclear plants, surgical implants, powder

technology, etc. Some classical notes can be found in [31, 32]. Several alloys are accessible like zinc plus copper named "brass", lead and tin named "solder," etc. "Nimonic 80A" is one of the super-alloys. Primary compositions are nickel and chromium. Nickel is induced by amount 69% where as chromium stands for 18%. Little amount of aluminium and titanium are introduced to make the alloy strengthened. Nimonic 80A alloys are extensively used in air craft [33], gas turbine manufacturing [34, 35] or automobile exhaust valves [36] or die-casting inserts and cores or nuclear boiler tube parts, fuel cells, marine diesel engine [37, 38], etc. This alloy explores high creep and rupture strength at elevated temperature. It holds superior corrosion as well as oxidation resistance. Heat transport investigation of carreau nanofluid flow runs over cone with Nimonic 80A particles was illustrated by Raju et al. [39]. Radiative MHD flow of alloy nanoparticles passed over revolving disc was reported by Makinde et al. [40]. A natural convective ethylene glycol Nimonic 80A nanoliquid stream run over vertical surface was demonstrated by Sandeep et al. [41]. Nimonic 80A nanoliquid suspension crossing over permeable stretching or shrinking cylindrical texture was depicted by Sandeep et al. [42]. Impression of shape factor of tiny Nimonic 80A particles with entropy analysis was discussed by Ellahi et al. [43].

The physical procedure in which molecules or particles combine together to construct long structure are termed as aggregates. It is an imperative branch of colloidal science and technology. Generally it is irreversible mechanism. But there is minor variation between agglomeration and aggregation. Aggregation refers to gathering of molecules in a specific pattern having strong bonding, but in agglomeration molecules are loosely joined and they can shatter using mechanical force. The formations of aggregation are recognized by fractal geometry. Enrichment of thermal conductivity of nanoliquid is fervently debatable topic. Recent reports extract that aggregation of nanocomposite performs key character in thermal performance of nanofluids. Keblinski et al. [44] recommended that particle's size, liquid–molecule interface plus aggregation of nanoparticles provide key enrichment aspects compared to Brownian movement of particles. Wang et al. [45] consumed experimental attempt to depict that aggregating feature of nanoparticle predicts efficient thermal conductivity. Influence of aggregation kinetics on thermal conductivity of nanosuspension was deliberated by Prasher et al. [46]. Impression of aggregated composite and interfacial hindrance on nanofluids was illustrated by Evans et al. [47]. Contribution of aggregated composite on unsteady mixed convective nanostream was investigated by Sui et al. [48]. The related literatures can be traced in [49–51].

Nanoparticles thermal conductivity can be significantly increased by means of aggregation. Additionally, there are several challenges associated with nanoparticles. One of the most significant challenges for engineers is to address how such molecular interaction like aggregation kinetics inside the system affects the thermophysical properties of the fluid. How heat transfer, engendered temperature or thermal conductivity can be affected due to aggregation kinetics is brought forwarded through this literature. Thus, in this paper we have explored the effect of aggregation kinetics on nanofluid inside a spinning channel under the light of preceding works. Upper segment of the channel is assumed to be permeable, but lower one stretches. Special Nimonic 80A tiny particles are suspended into water to construct nanosolution. Main equations have been tackled via RK-4 method in conjunction of shooting strategy. Several graphs and tables have been employed to extract fine points of the investigation. We hope our unique attempt will acquire a novel corner in technological aspects.

Mathematical formulation

Leading equations and boundary conditions

Let us consider an incompressible flow of water-based nanofluid between two infinite plates in a revolving frame of reference with angular velocity $\boldsymbol{\Omega} = (0, \Omega, 0)$. The model has been constructed so as to have a permeable plate in upper direction and a stretching plate at lower portion with stretched velocity $U_w = bx$ where $b > 0$. The velocity structure of the fluid has been taken as $U(u, v, w)$ along the (x, y, z)-axis, respectively. The temperature of the upper plate is confined with temperature T_0, and the same is T_h for lower plate having the condition $T_0 < T_h$ as depicted in Fig. 1. We have assembled our investigation on behalf of some physical assumption that chemical reaction or radiative heat transfer is absent between nanoparticles and water, and no slips (thermal jump or velocity slip) take place between them. Viscous dissipation or joule heating is ignored. All body forces are neglected. Here we have used a special type of nanoparticles called Nimonic 80A alloy nanoparticles. Thermophysical features of base fluid including nanoparticles following [41] are enlisted in Table 1. Under these circumstances, the governing equations following [23–26] can be framed as follows:

$$\frac{\partial u}{\partial x} + \frac{\partial v}{\partial y} + \frac{\partial w}{\partial z} = 0 \tag{1}$$
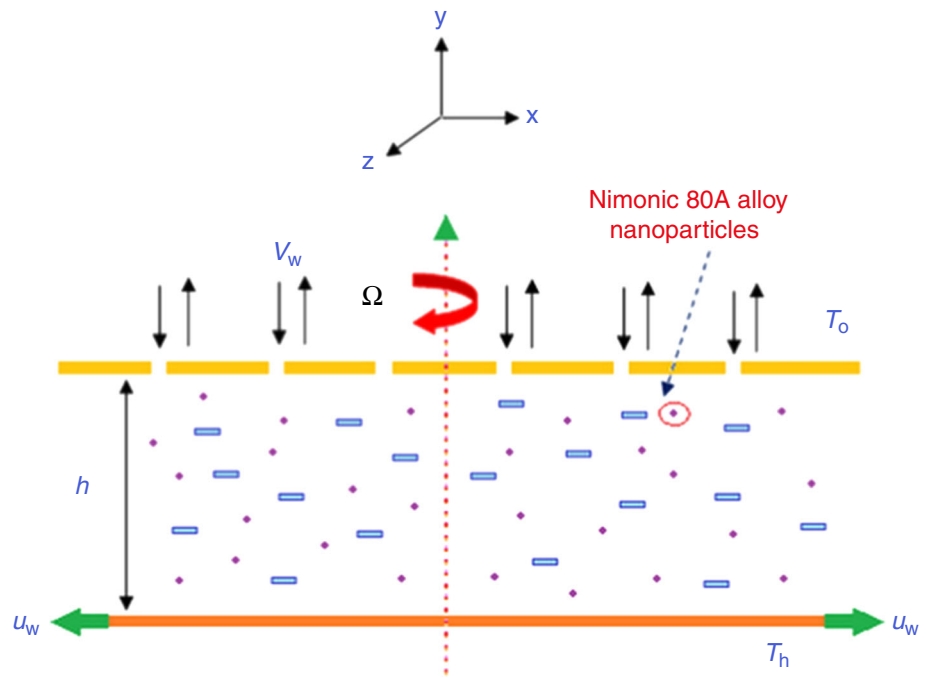
Fig. 1 Schematic of the problem

Table 1 Thermophysical properties of base fluid and nanoparticles

Physical properties	Water	Nimonic 80A
C_p/J kg^{-1} K^{-1}	4179	448
ρ/kg^{-1} m^{-3}	997.1	8190
κ/W^{-1} mK^{-1}	0.613	112

$$\rho_{nf}\left(u\frac{\partial u}{\partial x} + v\frac{\partial u}{\partial y} + 2\Omega w\right) = -\frac{\partial p^*}{\partial x} + \mu_{nf}\left(\frac{\partial^2 u}{\partial x^2} + \frac{\partial^2 u}{\partial y^2}\right) \quad (2)$$

$$\rho_{nf}\left(u\frac{\partial v}{\partial x} + v\frac{\partial v}{\partial y}\right) = -\frac{\partial p^*}{\partial y} + \mu_{nf}\left(\frac{\partial^2 v}{\partial x^2} + \frac{\partial^2 v}{\partial y^2}\right) \quad (3)$$

$$\rho_{nf}\left(u\frac{\partial w}{\partial x} + v\frac{\partial w}{\partial y} - 2\Omega u\right) = \mu_{nf}\left(\frac{\partial^2 w}{\partial x^2} + \frac{\partial^2 w}{\partial y^2}\right) \quad (4)$$

$$u\frac{\partial T}{\partial x} + v\frac{\partial T}{\partial y} + w\frac{\partial T}{\partial z} = \alpha_{nf}\left(\frac{\partial^2 T}{\partial x^2} + \frac{\partial^2 T}{\partial y^2} + \frac{\partial^2 T}{\partial z^2}\right) \quad (5)$$

where $p^* = p - \frac{\Omega^2 x^2}{2}$ denotes the modified pressure. It is noteworthy to note that non-existence of $\frac{\partial p^*}{\partial z}$ confirms net cross-flow along z-axis.

The requisite boundary constraints consist of

$$\left.\begin{array}{l} u = U_w = bx, v = 0, w = 0, T = T_h \text{ at } y = 0 \\ u = 0, v = -v_w, w = 0, T = T_0 \text{ at } y = h \end{array}\right\} \quad (6)$$

where $v_w > 0$ indicates suction and $v_w < 0$ represents injection at the upper surface.

Aggregation outline

It has already been explored experimentally that nanofluids are blessed with elevated thermal conductivity (κ). Now enhancement in κ can be possibly acquired by Brownian movement of nanoparticles [52, 53] or due to aggregation of petite nanoparticles leading to local percolation behaviour [44, 54]. Figure 2 schematically depicts aggregation scenario. The possibility of aggregation amplifies with reducing particle's size at continuous volume fraction, because these would diminish inter-particle distance, causing the van der Waals force more attractive [55]. Basically Brownian randomness decreases owing to aggregation which enhances the mass of aggregates, whereas percolation characteristics of aggregates can
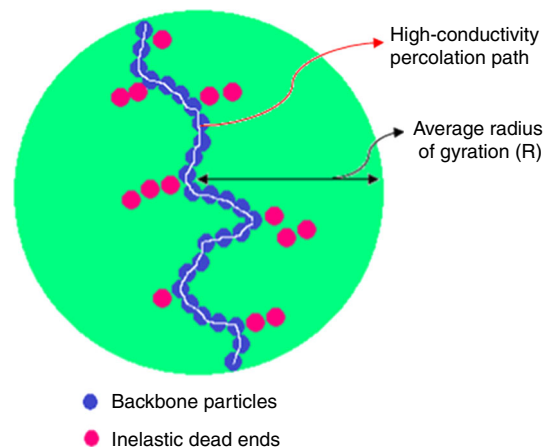

Fig. 2 Aggregation of nanoparticles

produce enormous increase in k, as super conducting particles get nearer to each other in aggregate. This section mainly enlightens the construction of aggregation kinetics for nanofluid flow. Basically aggregation approach allows us to redefine thermophysical features of nanofluid. For Eqs. (2)–(5), the following thermophysical features $\rho_{nf}, (\rho C_p)_{nf}, \mu_{nf}$ and κ_{nf} are defined [47] as:

$$\rho_{nf} = (1 - \phi_a)\rho_f + \phi_a\rho_a \tag{7}$$

$$(\rho C_p)_{nf} = (1 - \phi_a)(\rho C_p)_f + \phi_a(\rho C_p)_a \tag{8}$$

$$\frac{k_{nf}}{k_f} = \frac{k_a + 2k_f - 2\phi_a(k_f - k_a)}{k_a + 2k_f + \phi_a(k_f - k_a)} \tag{9}$$

$$\mu_{nf} = \mu_f\left(1 - \frac{\phi_a}{\phi_{max}}\right)^{-2.5\phi_{max}} \tag{10}$$

Now the thermal characteristics of particles aggregation are demonstrated as:

$$\rho_a = (1 - \phi_{int})\rho_f + \phi_{int}\rho_s \tag{11}$$

$$(C_p)_a = (1 - \phi_{int})(C_p)_f + \phi_{int}(C_p)_s \tag{12}$$

Tiny nanoparticles immersed into base liquid would aggregate among each other to figure out chain structure, which has been established experimentally [56]. There are two parts in this aggregation: One is the linear chain which spans the entire aggregate named backbone particles and second which does not contribute themselves to span the complete aggregate classified as dead ends. In the rheology of colloids, backbone performs a very noteworthy function because it is the only configuration that can transport elastic forces among aggregate. Owing to its connectivity, the backbone particles are expected to contribute an essential role in thermal conductivity. Figure 2 illustrates the schematic of a single aggregate that includes backbone as well as dead-end particles [46, 47]. To address further on the consequence of aggregation, thermal conductivity is reframed by means of fractal theory.

Therefore, to determine thermal conductivity of aggregate we need to separate it into two components: first is the percolation contributing factor, i.e. backbone, and next one is non-percolation contributing dead ends. Taking into account of the interfacial thermal resistance, i.e. Kapitza resistance, the thermal conductivity of dead-end particles (counting base fluid and dead-end particles) is calculated by [46]:

$$\frac{(1 - \phi_{nc})(\kappa_f - \kappa_{nc})}{(\kappa_f + 2\kappa_{nc})} + \frac{\phi_{nc}(\kappa_s - \kappa_{nc})}{(\kappa_f + 2\kappa_{nc})} = 0 \tag{13}$$

The effective thermal conductivity of the aggregate including the particles belonging to the backbone is calculated by assuming that the backbone is embedded in a medium with an effective conductivity of κ_{nc}. Since the

aspect ratio of the chains is significantly larger than one, we use the model by Nan et al. [57] for randomly oriented cylindrical particles. Using Nan's model, the effective thermal conductivity of the aggregate sphere, κ_a, with both the chains and dead ends (Fig. 2) is given by:

$$\kappa_a = \kappa_{nc}\frac{3 + \phi_c\{2\beta_{11}(1 - L_{11}) + \beta_{33}(1 - L_{33})\}}{3 - \phi_c\{2\beta_{11}L_{11} + \beta_{33}L_{33}\}} \tag{14}$$

where

$$\left.\begin{array}{l}L_{11} = \dfrac{0.5p^2}{(p^2 - 1)} - \dfrac{0.5p\cosh^{-1}p}{(p^2 - 1)^{1.5}} \\[3mm] L_{33} = 1 - 2L_{11}, \quad \beta_{ii} = \dfrac{\kappa_{ii}^c - \kappa_{nc}}{\kappa_{nc} - L_{ii}(\kappa_{ii}^c - \kappa_{nc})}\end{array}\right\} \tag{15}$$

Also interfacial resistance is termed as:

$$\kappa_{ii}^c = \frac{\kappa_s}{\left(1 + \gamma L_{ii}\frac{\kappa_s}{\kappa_f}\right)} \tag{16}$$

where $\gamma = \left(2 + \frac{1}{p}\right)\alpha$, $\alpha = \frac{A_k}{a}$. The term p that appears in (15) indicates aspect ratio, for which the cluster linear spanning chain is provided by $p = \frac{R}{a}$. It is to be noted that our investigation permit us to capture the features of cluster morphology by means of three factors R, d_f and d_l.

Now the aggregation number of involved particles is defined as $N_{int} = \left(\frac{R}{a}\right)^{d_f}$ Because of number conservation of nanoparticles, $\phi = \phi_{int}\phi_a$. It has been showed [46] that $\phi_{int} = \left(\frac{R}{a}\right)^{d_f - 3}$ and $\left(\frac{R}{a}\right)_{max} = \phi^{\frac{1}{d_f - 3}}$ [58] for which $\phi_a = 1$. The amount of particles included to form backbone structure, i.e. N_c, is expressed by [59] $N_c = \left(\frac{R}{a}\right)^{d_l}$. It is important to note that $d_l = d_f$, which confirms the fact that all particles fit in the backbone; consequently, there do not exist dead ends. Hence, volume fraction of particles involved in backbone is defined as $\phi_c = \left(\frac{R}{a}\right)^{d_l - 3}$, but same for dead ends can be constructed as $\phi_{nc} = \phi_{int} - \phi_c$.

Finally, the thermal conductivity for the entire structure following [45] and [46] is evaluated via the Maxwell–Garnet (M–G) model. Therefore, the required thermal conductivity of the complete system is described [60] by

$$\kappa_{eff} = \kappa_f\left\{\frac{(\kappa_a + 2\kappa_f) + 2\phi_a(\kappa_a - \kappa_f)}{(\kappa_a + 2\kappa_f) - \phi_a(\kappa_a - \kappa_f)}\right\} \tag{17}$$

Non-dimensional approach

Now we implement the following function to convert governing equations into its dimensionless form:

$$\left.\begin{array}{l}u = bxf'(\eta), v = -bhf(\eta), w = bxg(\eta) \\[2mm] \theta(\eta) = \dfrac{T - T_0}{T_h - T_0}, \eta = \dfrac{y}{h}\end{array}\right\} \tag{18}$$

Using (18) and omitting pressure gradient (2)–(5) transforms as:

$$f^{\text{iv}} - \delta \frac{A_1}{A_2}(f'f'' - ff''') - 2\lambda \frac{A_1}{A_2}g' = 0 \qquad (19)$$

$$g'' - \delta \frac{A_1}{A_2}(gf' - fg') + 2\lambda \frac{A_1}{A_2}f' = 0 \qquad (20)$$

$$\theta'' + Pr \frac{A_3}{A_4}\delta f \theta' = 0 \qquad (21)$$

where

$$\left. \begin{array}{l} A_1 = (1 - \phi_{\text{a}}) + \phi_{\text{a}}\dfrac{\rho_{\text{a}}}{\rho_{\text{f}}}, \ A_2 = \dfrac{1}{(1 - \phi_{\text{a}})^{2.5}} \\[2mm] A_3 = (1 - \phi_{\text{a}}) + \phi_{\text{a}}\dfrac{(\rho C_{\text{p}})_{\text{a}}}{(\rho C_{\text{p}})_{\text{f}}}, \ A_4 = \dfrac{\kappa_{\text{eff}}}{\kappa_{\text{f}}} \end{array} \right\} \qquad (22)$$

Also boundary conditions are reframed as:

$$\left. \begin{array}{l} f(0) = 0, f'(0) = 1, g(0) = 0, \theta(0) = 1 \\ f(1) = S, f'(1) = 0, g(1) = 0, \theta(1) = 0 \end{array} \right\} \qquad (23)$$

where $S > 0$ indicates suction and $S < 0$ signifies injection.

Engineering quantities

The requisite aspects of engineering interest are C_{f} and Nu. They are defined as follows:

$$\left. C_{\text{f}} = \dfrac{\mu_{\text{nf}}\left(\frac{\partial u}{\partial y}\right)}{\frac{\rho_{\text{nf}}U_{\text{w}}^2}{2}}\right|_{\text{y}=0\,\text{or}\,h}, \ Nu = \dfrac{-x\kappa_{\text{eff}}\left(\frac{\partial T}{\partial y}\right)}{\kappa_{\text{f}}(T_{\text{w}} - T_\infty)}\right|_{\text{y}=0\,\text{or}\,h} \right\} \qquad (24)$$

Now employing similarity technique in (24) C_{fr} and Nu_{r} can be reframed as

$$C_{\text{fr}} = C_{\text{f}}Re_{\text{x}}^{\frac{1}{2}} = \left. \dfrac{f''(\eta)}{\left[(1 - \phi_{\text{a}}) + \phi_{\text{a}}\frac{\rho_{\text{a}}}{\rho_{\text{f}}}\right](1 - \phi_{\text{a}})^{2.5}} \right|_{\eta\,=\,0\,\text{or}\,1} \qquad (25)$$

$$Nu_{\text{r}} = Nu \cdot Re_{\text{x}}^{-\frac{1}{2}} = \left. -\dfrac{\kappa_{\text{eff}}}{\kappa_{\text{f}}}\theta'(\eta) \right|_{\eta\,=\,0\,\text{or}\,1} \qquad (26)$$

where $y = 0\,\text{or}\,h$ and $\eta = 0$ or 1 signifies lower and upper portion of the plate, respectively.

Numerical implementation

Methodology

Now, we execute the coupling nonlinear ODEs (19)–(21) together with boundary conditions (23) by switching the

problem to an initial value procedure. Equations (19)–(21) can be reframed as the set of first-order ODEs as follows:

$$\left. \begin{array}{l} f' = z \\ z' = p \\ p' = q \\ g' = l \\ q' = \delta \dfrac{A_1}{A_2}(zp - fq) + 2\lambda \dfrac{A_1}{A_2}l \\ l' = \delta \dfrac{A_1}{A_2}(gz - fl) - 2\lambda \dfrac{A_1}{A_2}z \end{array} \right\} \qquad (27)$$

and

$$\left. \begin{array}{l} \theta' = r \\ r' = -Pr\dfrac{A_2}{A_3}\delta fr \end{array} \right\} \qquad (28)$$

Thus, to integrate the system we need the values of

$$\left. \begin{array}{l} z(0) = f'(0), \ p(0) = f''(0), \ q(0) = f'''(0), \\ l(0) = g'(0), \ r(0) = \theta'(0) \end{array} \right\} \qquad (29)$$

From the given boundary proviso, we have acquired the values of only $f'(0)$. Hence, in the absence of rest of the values, we have to make some suitable guesses of $f''(0), f'''(0), g'(0), \theta'(0)$. Then, integration is performed and compared with the numerical values of $f(0), g(0), \theta(0), f(1), f'(1), g(1), \theta(1)$. We alter the data of $f''(0), f'''(0), g'(0), \theta'(0)$ to achieve better approximate solution. We implement RK-4 method on the series of values of $f''(0), f'''(0), g'(0), \theta'(0)$ considering the step size as $h = 0.01, 0.001, \ldots\ldots$ etc. The internal iteration is finished with the convergence criterion 10^{-6} in all cases.

Authentication of the present study

In order to authenticate the accuracy of our present investigation, we have compared our model in two ways. First to authenticate our simulation-based modelling, we depicted the temperature profile for various values of Prandtl number with those as reported by Sheikholeslami et al. [25]. Temperature profile is plotted in Fig. 3. Clearly it explores excellent agreement. Again to verify our results with experimental data, we have captured the numeric values of skin friction for Al_2O_3–water (alumina–water) nanofluid flow in micro-channels considering the absence of rotation, for various values of Reynold's number δ in Fig. 4. It depicts good agreement with previously performed experimental set-up by Bowers et al. [18].
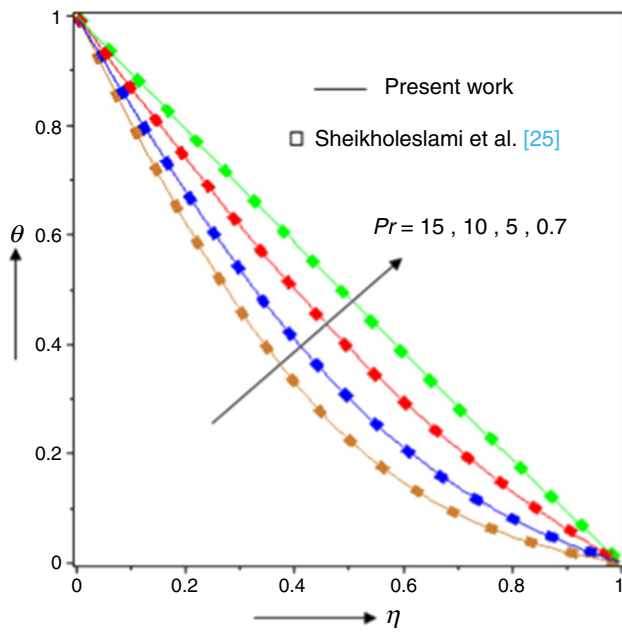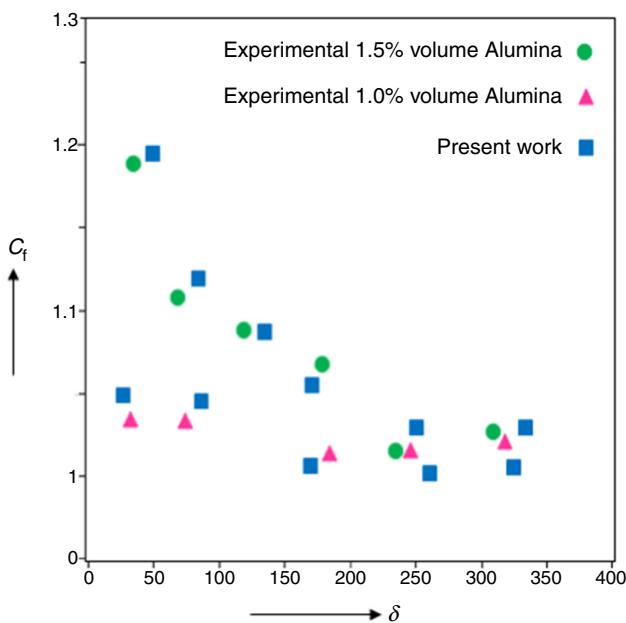
Fig. 3 Comparison with numerical simulation

Fig. 4 Comparison with experimental data

Results and discussions

The present section addresses the parametric study of the flow profile. The section will enlighten the effect of various parameters on velocity, temperature and effective thermal response via graphs and tables. Frictional coefficient and heat transfer will also find an important corner in this discussion. To divulge the graphical features, we have assigned the values of parameters as $\delta = 2.0, S = 1.0, \lambda =$

2.0 unless otherwise specified. In our simulation, we have opted water as a base solution. Pandtl number (Pr) varies from 5.6 to 10 for water at usual room temperature. But Pr is a function of volume fraction that is why when nanoparticle volume fraction changes, its value reduces by particle loading [22]; hence, it cannot be assumed constant. Also when we add nanoparticles in the solution, the aggregative features of nanocomposite provide enormous increase in effective thermal conductivity of base fluid [46], and consequently, $Pr = \frac{\mu C_p}{\kappa}$ will reduce. In this numerical simulative work, we choose those values as $Pr = 6.2$ when $\phi = 0.00, Pr = 5.2$ when $\phi = 0.01, Pr = 4.2$ when $\phi = 0.02$.

Effect of fractal dimension (d_f)

Consequences of fractal dimension d_f on velocity profile, i.e. on $f'(\eta), g(\eta)$, are illustrated in Fig. 5. The spherical shaped tiny particles with radius 10 nm are considered. Also we have presumed 50 particles which belong to backbone in single aggregation with radius of gyration 150 nm. When total 100, 200 and 300 particles share themselves in single aggregation, the values of d_f are found to be 1.70, 1.95 and 2.10, respectively. Figure 5a depicts that inside the channel initially $f'(\eta)$ increases within $0.0 \leq \eta \leq 0.5$ (not precisely determined) and effect is undoubtedly distinct. But approximately at the middle of the path say $\eta = 0.5$, a sudden switch over is noticed. The initial output exhibits enhancement in velocity, but it is transparent that due to the amplification of aggregate's size, the relative viscous effect will enhance. Additionally, the contour of the aggregates will not preserve its spherical appearance owing to aggregation, because the inherent viscosity would be greater than 2.5 for other shapes. This indicates that preliminary increase in $f'(\eta)$ at the proximity of the wall causes to reduce velocity gradient. But to conserve mass flow rate, finally reduction in fluid velocity near the wall will be compensated by the decreasing fluid velocity near the central region. That is why reverse scenario is observed. It also informs us that speed of nanofluid will be diminished when enhancement of number of particles in aggregations is found. Enormous increment in $g(\eta)$ is detected for increasing d_f. In the midst of the path, high impact is perceived. Moreover, value of d_f from 1.70 to 1.95 provides high impact inside flow regime. In Fig. 5a, b, amplifying nanoparticle volume fractions lead to reduce velocity comparatively. In both volumetric situations ($\phi = 0.01$ and $\phi = 0.02$), lower portion of the surface experiences raising frictional features. Table 2 confirms that same is true for upper face. Comparatively, 5.06% augmentation in C_{fr} is noticed for lower portion. Thus,
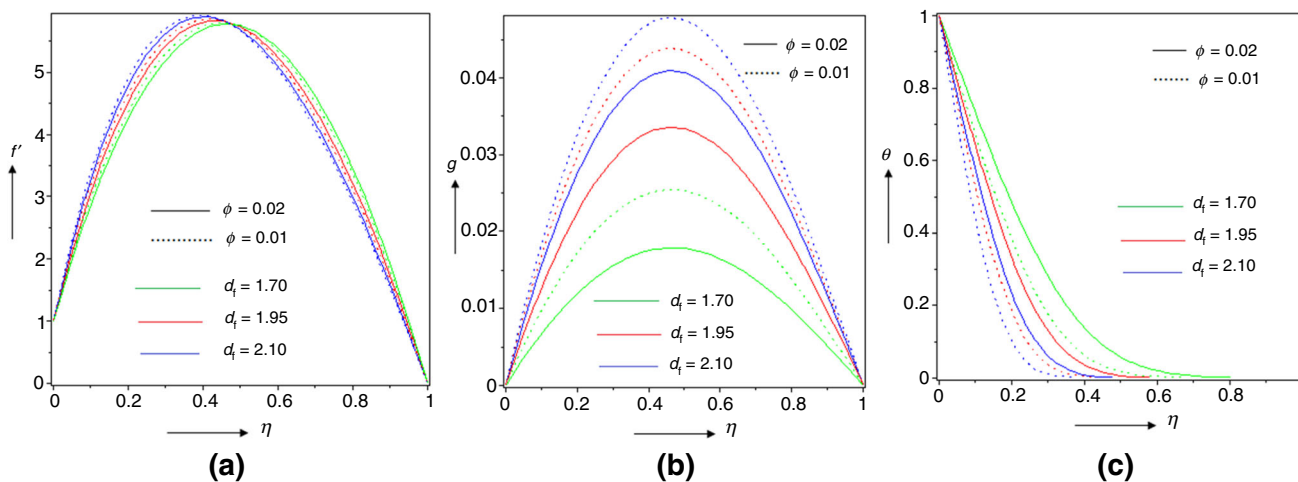
Fig. 5 Effect of d_f on velocity and temperature

Table 2 Values of C_{fr} for various aggregation parameters

d_f	d_l	R	C_{fr}			
			$\phi = 0.01$		$\phi = 0.02$	
			Lower surface	Upper surface	Lower surface	Upper surface
1.70			1.899278	− 3.608401	1.870054	− 3.640442
1.95			1.995260	− 3.508032	1.957874	− 3.545530
2.10			2.094743	− 3.413752	2.057009	− 4.008304
	1.45		3.173847	− 4.849164	2.998086	− 4.716195
	1.70		3.265461	− 4.754957	3.091966	− 4.616984
	1.85		3.348200	− 4.674357	3.176988	− 4.531159
		100	3.475365	− 5.121650	3.281287	− 4.984682
		150	3.760432	− 4.844033	3.455007	− 4.803660
		200	4.077966	− 4.587347	3.685249	− 4.592886

lower face will be mostly drag affected at low volume fraction.

Figure 5c explores significant diminution in temperature profile. Inside $0.0 \leq \eta \leq 0.6$ (not accurately determined), outcome sounds well. Actually raising d_f aids dead-end particles to increase in number. We know that dead-end molecules do not contribute themselves in high conductive percolation path. Hence temperature drops off. Additionally increasing volume fraction provides the base liquid to consume more tiny particles; consequently, efficient thermal performance helps to swell the temperature inside the flow province. Thus, fluid blessed with comparatively low volume fraction acquires less temperature. Involvement of high fractal factor promotes heat transfer rate at lower portion of the channel. Lower portion offers maximum heat transport features at $\phi = 0.01$. Opposite trend is perceived at upper surface.

Effect of chemical dimension (d_l)

Figure 6a, b indicates the impact of chemical dimension d_l on $f'(\eta), g(\eta)$. For constructing these profiles, we consider total 200 particles in aggregation, which are extended along 150 nm diameter. The values of d_l are 1.45, 1.70 and 1.85, taking 50, 100 and 150 molecules in backbone. Similar scenario in $f'(\eta)$ is exhibited for d_l as it was for d_f in Fig. 4a. But effect is not so distinct. Cause of this dual feature is same as given in section "Effect of fractal dimension (d_f)". Besides, outstanding distinct amplification is seen in $g(\eta)$ inside the region. The initial input data of d_l exhibit slight impact, but when value of d_l jumps from 1.45 to 1.70, 200% increment in $g(\eta)$ is observed. The presence of excess nanoparticle volume fractions generally cuts down the magnitude of $g(\eta)$. Maximum velocity is obtained at the mid-portion of the path. Inside $0.0 \leq \eta \leq 0.5$, the curve exhibits increasing nature. Beyond that regime, curve decreases effortlessly. Frictional effect is found to flourish at both surfaces as shown in Table 2.
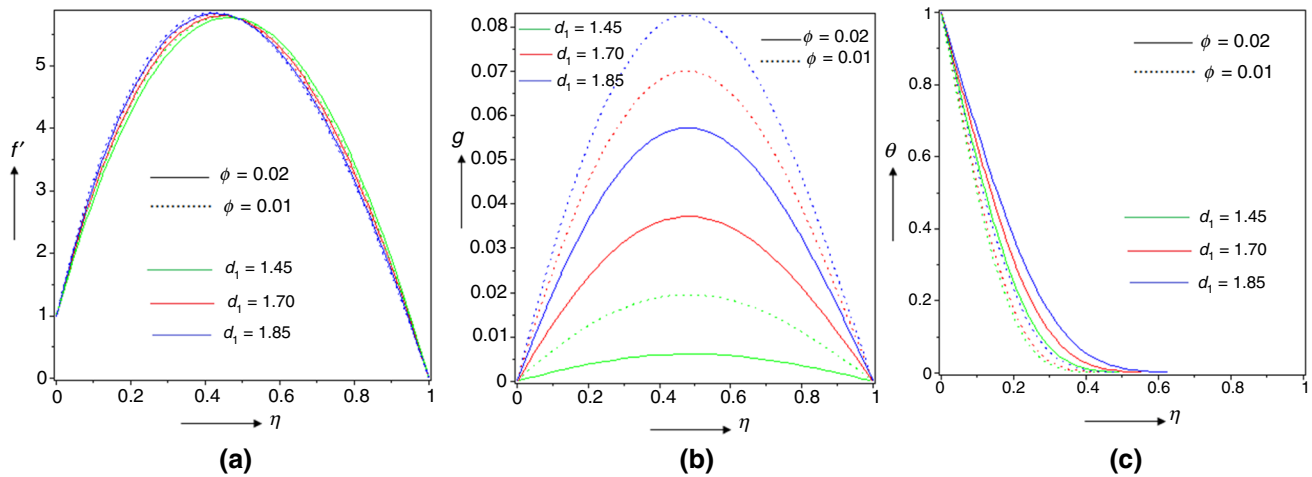
Fig. 6 Effect of d_l on velocity and temperature

But impressive influence is perceived at lower surface. At $\phi = 0.01$, augmentation in C_{fr} is perceived as 2.88%, whereas it is 2.13% for $\phi = 0.02$. At the upper portion, same is detected as 1.94% approximately. Thus, lower segment will be more frictionally affected.

Influence of d_l on temperature is demonstrated in Fig. 6c. Temperature rises inside the regime. Near the edge of the surface such consequence is effective, but far away from that portion such effect is wiped out. Clear outcome is perceived inside $0.0 \leq \eta \leq 0.4$ (not accurately determined). Physically increasing values of d_l confirms us about the escalating number of backbone molecules in the aggregate which offers enhancement in temperature. High volume fraction is detected to describe maximum temperature. Table 3 portrays slight growth in heat transfer at the upper surface. Comparatively for $\phi = 0.02$ rate of enhancement in Nu_r is high. It is about 90.55%. But reverse trend has been pointed out for lower face.

Effect of radius of gyration (R)

Impact of radius of gyration R on velocity profiles is portrayed in Fig. 7a, b. These profiles are arranged by taking 200 elements in aggregation, and every aggregation includes 150 dead-end nanoparticles, where 50 particles correspond to backbone structure, which are stretched along various radii. Figure 7a demonstrates the same features of $f'(\eta)$ as before. Same is true for $g(\eta)$ in Fig. 7b. In both situations, impacts are perceptible. In the midst of the way, impacts are sensitive. But the fluctuation in each curve of $g(\eta)$ as we have perceived before was high. In this case, such deviation is not so high. Both surfaces will experience increasing friction at each volumetric condition. Table 2 predicts that lower region aids 8.20% increment at 1% nanoparticle volumetric fraction, but 2% volumetric situation depicts 5.29%. Additionally, 5.42% increment was illustrated by upper region at low volumetric profile, but 3.67% was detected for rest one. Thus, texture of both

Table 3 Values of Nu_r for various aggregation parameters

| d_f	d_l	R	Nu_r			
			$\phi = 0.01$		$\phi = 0.02$	
			Lower surface	Upper surface	Lower surface	Upper surface
1.70			1.796851	0.175355	1.509961	0.367200
1.95			2.717696	0.009162	1.996747	0.117644
2.10			3.314279	0.006326	2.428098	0.034511
	1.45		2.512487	0.013217	2.413983	0.047189
	1.70		2.400211	0.052163	2.293561	0.089921
	1.85		2.197605	0.103631	2.076328	0.147120
		100	3.005762	0.002722	2.336814	0.052089
		150	2.464576	0.023421	1.923181	0.152537
		200	1.867264	0.145705	1.467442	0.413324
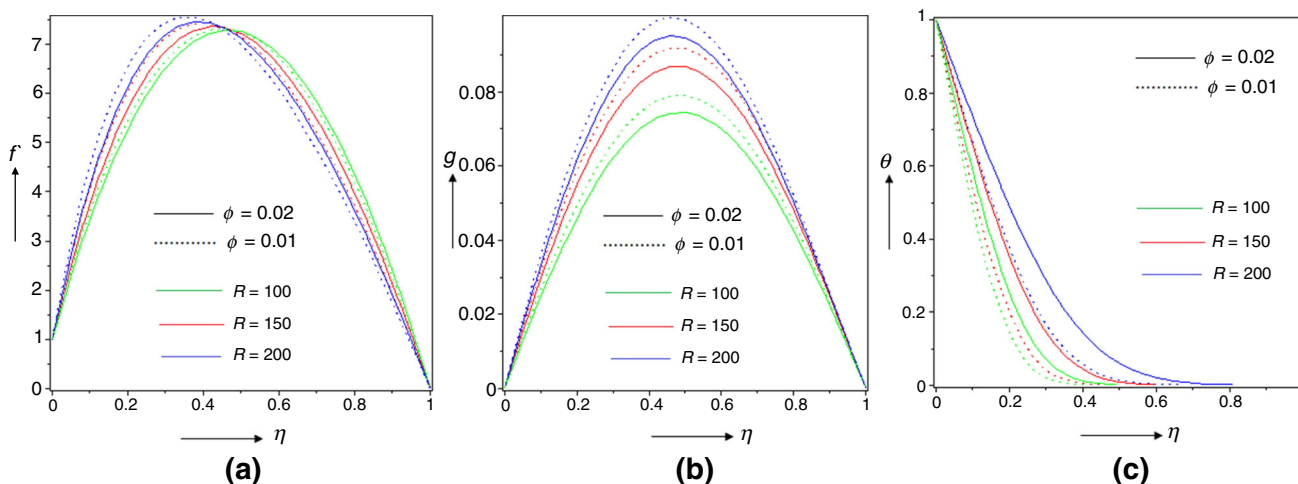
Fig. 7 Effect of R on velocity and temperature

surfaces will be drag affected if we do not restrict R properly.

Again temperature illustrates fine amplification in Fig. 7c inside flow regime. For increasing R, profile explores clear appearance inside $0.0 \leq \eta \leq 0.8$. After that, it assures far field proviso. Physically backbone particles spreading over long radius facilitate their rheological features to enhance temperature. Also higher volumetric criteria of tiny particles generate more temperature compared to lower one. Table 3 describes reducing heat transport mechanism in lower portion of the path. But opposite inclination is confirmed for upper face. Comparatively larger volumetric concentration grants high rate of Nu_r in upper region. This is quite reasonable because when connecting particles along backbone structure spread in big radius, heat transfer gets improved as compared to backbone in little radius.

Effect of Kapitza interfacial resistance on effective thermal conductivity

The function of interfacial resistance for aggregated configuration is illustrated in Fig. 8. It detects that interfacial resistance cuts the effective thermal conductivity of the structure. Without aggregation and interestingly Kapitza radius equivalent to particle diameter, there correspond no thermal conductivity increment. However, with escalating cluster size more benefits of elevated conductivity are realized. Interfacial resistance or Kapitza resistance denotes the interface hindrance against thermal flow. It offers a barricade towards heat flow. Extension of Fourier's law provides us $Q = \frac{\Delta T}{R_r}$, where Q denotes heat flux, R_r indicates interfacial resistance and ΔT corresponds temperature drop. Assuming Q as constant, the above formula depicts a finite temperature discontinuity is caused by R_r.
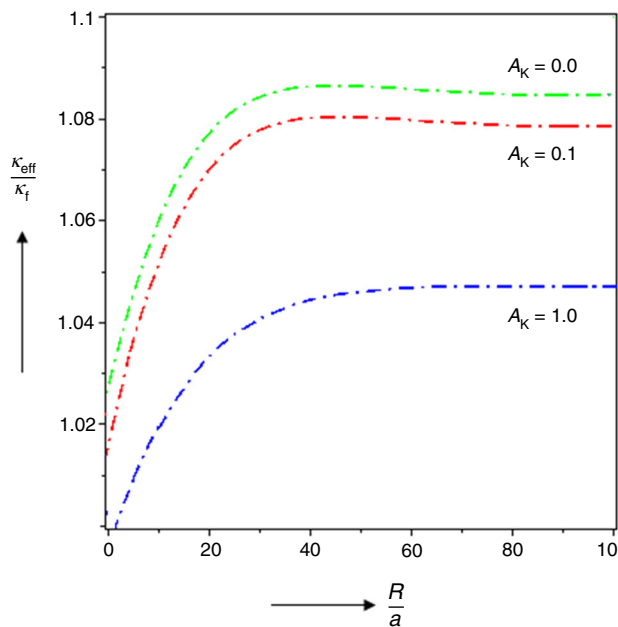

Fig. 8 Effect of Kapitza resistance on $\frac{\kappa_{eff}}{\kappa_f}$

Again for fully dispersed nanoparticles of radius r and Kapitza radius A_k, at low volume fractions theories [61] predict that:

$$\frac{\kappa_{eff}}{\kappa_f} = 3f\left(\frac{\frac{r}{A_k} - 1}{\frac{r}{A_k} + 2}\right) + 1 \tag{30}$$

It is lucid from (30) that increment in A_k will definitely reduce effective thermal responses. But there is no enhancement in thermal conductivity if $r = A_k$. For tiny particles, when $\frac{r}{A_k}$ is very small, interfacial resistance may be a decisive factor. However, in particles with small radii coinciding with larger interfacial hindrance, the

conductivity of the composite can be significantly reduced such as carbon nanotubes with single wall.

Effect of particle volume fraction on effective thermal conductivity

Figure 9 corresponds that increasing particle volume fraction leads to acquire high effective thermal conductivity. It is, moreover, significant that for any fixed volumetric fraction (say $\phi = 0.02$) the initial increase in aspect ratio or aggregate size offers definite amplification in effective conductivity, but saturates after some times. Physically increasing aspect ratio includes more backbone particles in the cluster which promotes effective conductivity across the composite. Once the composite started to overlap, aggregates response to its maximum conduction and after that it is saturated.

Effect of Reynold's number (δ)

Impact of Reynold's number on velocity profiles is demonstrated in Fig. 10a, b. Influence of both the presence and absence of aggregation is deliberated through graphs. In Fig. 10a, profile of $f'(\eta)$ explores the initial increment, but after a certain episode reverse outcome is noticed. Stretching at lower portion is the keen factor to make this happen. Curve rises inside $0.0 \leq \eta \leq 0.3$(not preciously determined), but after that profile drops off. More interestingly, maximum velocity is reached near lower surface of the wall. Improvization of δ aids the peak value to transfer itself more

Fig. 9 Effect of ϕ on $\frac{\kappa_{\text{eff}}}{\kappa_{\text{f}}}$

towards lower wall. Figure 10b portrays uniform reducing features inside the channel. Again maximum value of $g(\eta)$ tends to switch itself towards lower surface with increasing δ. Physically Reynolds number is the ratio among inertial force and viscous force. Thus, larger values of δ explore dominant features of inertial force as compared to viscous force. Consequently, velocity drops off. In Fig. 9a, aggregating structure discloses elevated velocity at the proximity of lower wall as compared to the absence of aggregation kinetics. But totally contradict scenario transpires in rest of the portion. But the deviation in these two phenomena is not so high or maximum. In Fig. 10b, velocity constantly gains less magnitude without aggregation. As compared to Fig. 9a, variations among aggregation and without aggregation in Fig. 10b are found to be more prominent. Friction provides swelling characteristics at both faces as shown in Table 4. 9.86% growth is detected at lower portion in aggregating state, but 19.26% augmentation is perceived in the absence of aggregation. For upper region, those are 3.61% and 36.51%, respectively.

Temperature drops off inside flow territory. Uniform reduction is noticed in Fig. 10c for $\phi = 0.02$. The absence of aggregation uplifts the temperature comparatively. Heat transfer has been detected to promote itself at lower region. But upper one delivers opposite symptom. Aggregation of molecule advances 18.07% enhancement at lower portion, while 31.76% growth is occupied without aggregation. Huge reduction has been acquired at upper wall. Numerically 95.56% is discovered in Table 5 for aggregation but 91.80% for without aggregating scenario.

Effect of rotational parameter (λ)

Figure 11a carries the influence of rotational factor λ on velocity $f'(\eta)$. Graph illustrates ups and downs inside the restricted regime. Near the lower wall ($0.0 \leq \eta \leq 0.3$), amplification in $f'(\eta)$ is recognized. But effect is not so prominent. Upper portion ($0.7 \leq \eta \leq 1.0$) provides the same. But in the mean spot quite reverse trend is noticed. Consequence is clear and distinct. The absence of rotation offers maximum velocity. Near lower and upper region non-existence of aggregation provides slight enhancement as compared to aggregated structure. But in the central region aggregated composite velocity runs high. It is essential to locate that only for $\lambda = 0.0$ uniform dual feature in $f'(\eta)$ is achieved because in this circumstance only at $\eta = 0.5$ switching behaviour of the presence and absence of affects the flow. Figure 11b signifies z-component velocity. Velocity increases inside the channel. Peak value is attained in the central portion. The absence of rotation converts the problem in 2D steady flow. Effect remains stagnant for $\lambda = 0.0$. Additionally, non-aggregated formation includes maximum speed. Table 4 assures C_{fr}
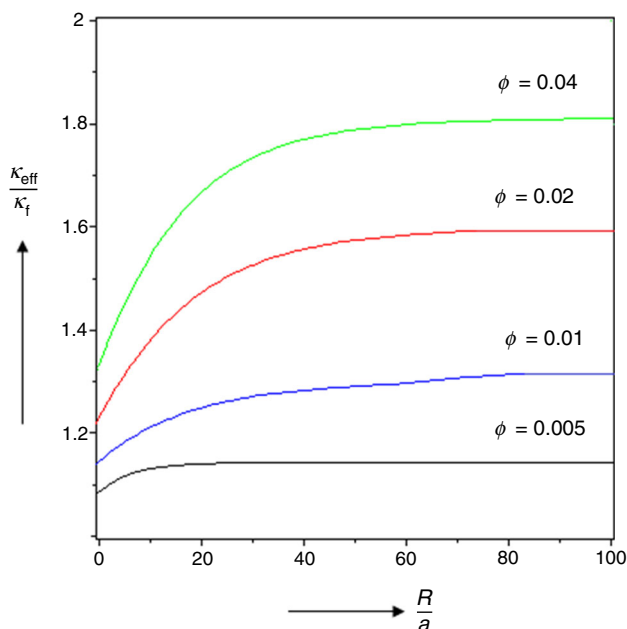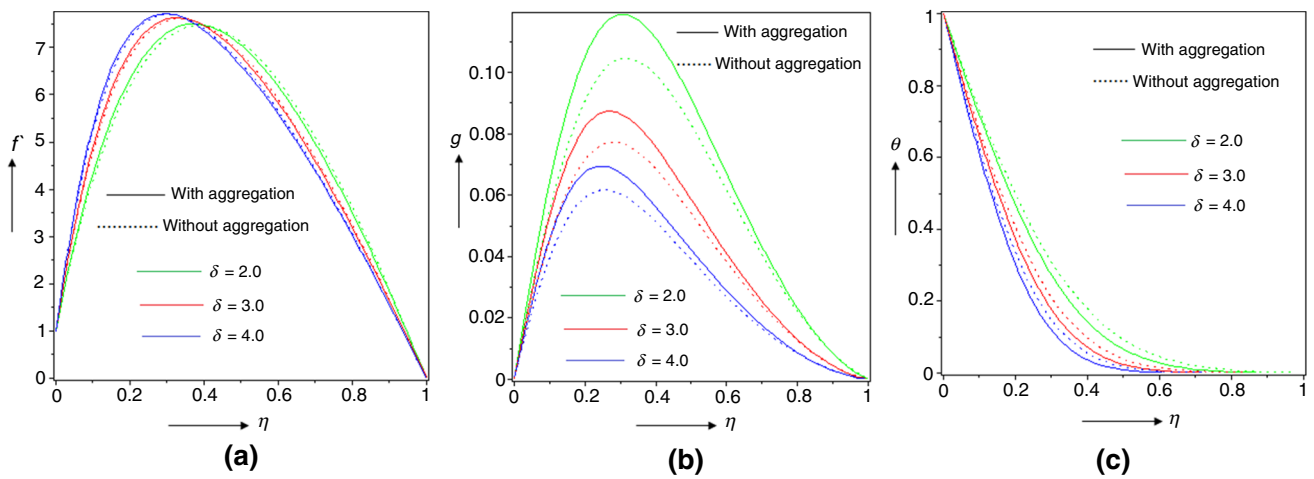
Fig. 10 Effect of δ on velocity and temperature

Table 4 Values of C_{fr} for various parameters

δ	S	λ	ϕ	C_{fr}			
				With aggregation		Without aggregation	
				Lower surface	Upper surface	Lower surface	Upper surface
2.0	1.0	2.0	0.02	4.077631	− 1.586511	3.525897	− 1.502369
3.0				4.479765	− 1.528687	4.201031	− 0.955354
4.0				5.127510	− 1.516419	5.109832	− 0.857956
2.0	0.0			− 3.676992	1.757495	− 3.178982	1.250683
	1.0			4.077631	− 1.586511	3.525897	− 1.502369
	2.0			5.353984	− 1.320569	6.328425	− 3.327881
	1.0	0.0		2.869866	− 2.713380	1.885614	− 0.615789
		2.0		4.077631	− 1.586511	3.525897	− 1.502369
		4.0		3.344246	− 3.617436	4.310383	− 3.987374
		2.0	0.00	4.511145	− 2.024826	3.160015	− 1.978741
			0.01	4.274251	− 1.746235	3.339917	− 1.711532
			0.02	4.077631	− 1.586511	3.525897	− 1.502369

Table 5 Values of Nu_{r} for various parameters

| δ	S	λ	ϕ	Nu_{r}			
				With aggregation		Without aggregation	
				Lower surface	Upper surface	Lower surface	Upper surface
2.0	1.0	2.0	0.02	2.251705	0.005295	2.854404	0.015394
3.0				2.658711	0.000235	3.761149	0.001261
4.0				3.516974	0.000017	4.152247	0.000117
2.0	0.0			1.368911	0.075257	1.541785	0.651247
	1.0			2.251705	0.005295	2.854404	0.015394
	2.0			2.686409	0.008017	3.306442	0.000624
	1.0	0.0		2.556250	0.000623	3.181303	0.000462
		2.0		2.251705	0.005295	2.854404	0.015394
		4.0		2.050466	0.037115	2.425997	0.035187
		2.0	0.00	2.532174	0.000157	3.052147	0.006324
			0.01	2.361705	0.002731	2.916142	0.011274
			0.02	2.251705	0.005295	2.854404	0.015394
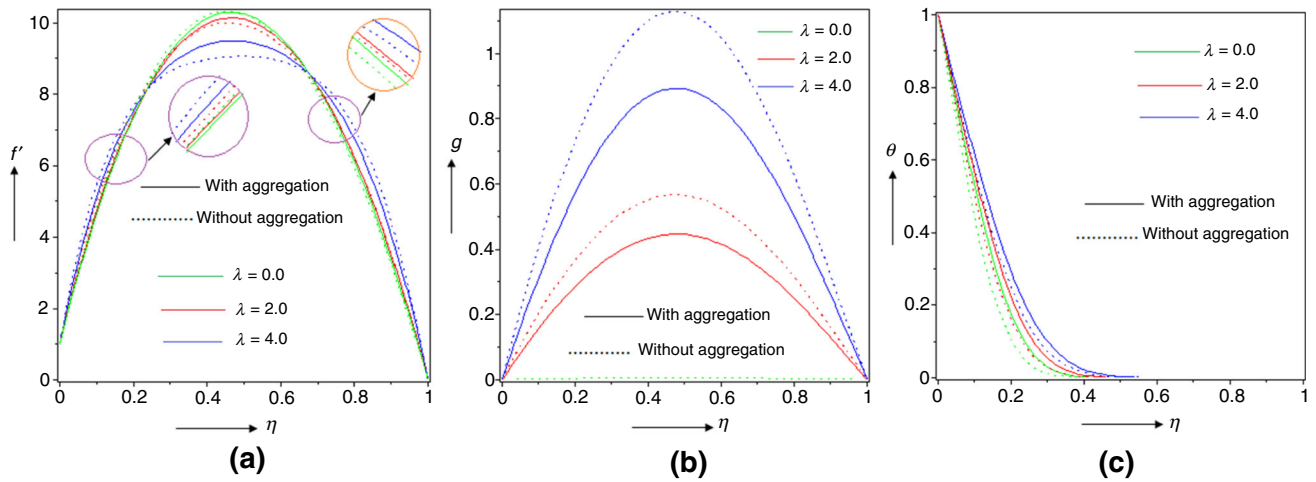
Fig. 11 Effect of λ on velocity and temperature

detonates at the upper regime, while opposite is true for lower one. Features hold the same for both formations of the flow.

Temperature escalates for rotational effect when $\phi = 0.02$. Figure 11c confirms prominent increment nearby lower portion of the channel. The presence of aggregation explores maximum temperature. Perhaps high conducting percolation path aids aggregated structure to contain high temperature. Heat transfer goes down at lower portion. 11.91% decay is seen for aggregating composite, while the rate is 10.27% for non-aggregated composite. At upper segment, Nu_r amplifies.

Effect of nanoparticle volume fraction (ϕ)

Figure 12a communicates the variation in $f'(\eta)$ due to ϕ. Decreasing scenario has been observed for lower half to middle portion owing to aggregated structure, but for rest

of the flow regime reverse scenario emerges. Effects are clear and distinct. Aggregating formation depicts less velocity distribution as compared to non-aggregating composition. More interestingly, reverse features are observed for non-aggregated molecules. Here velocity amplifies. Maximum velocity is gained at the middle segment for aggregated molecules, whereas for non-aggregated structure this value is slightly switched to the lower portion. For aggregation, regular fluid gains maximum speed inside $0.0 \leq \eta \leq 0.5$, whereas non-aggregated liquid explores the opposite. Figure 12b depicts reducing velocity profile for both features. Curve portrays increasing property up to mid-portion of the channel, but from then it exposes decreasing features. This time also non-aggregated formation occupies comparatively high velocity. But regular fluid possesses highest velocity. The presence of aggregation assists C_{fr} to reduce at both surfaces, but the absence of aggregation confirms the opposite. Thus, from
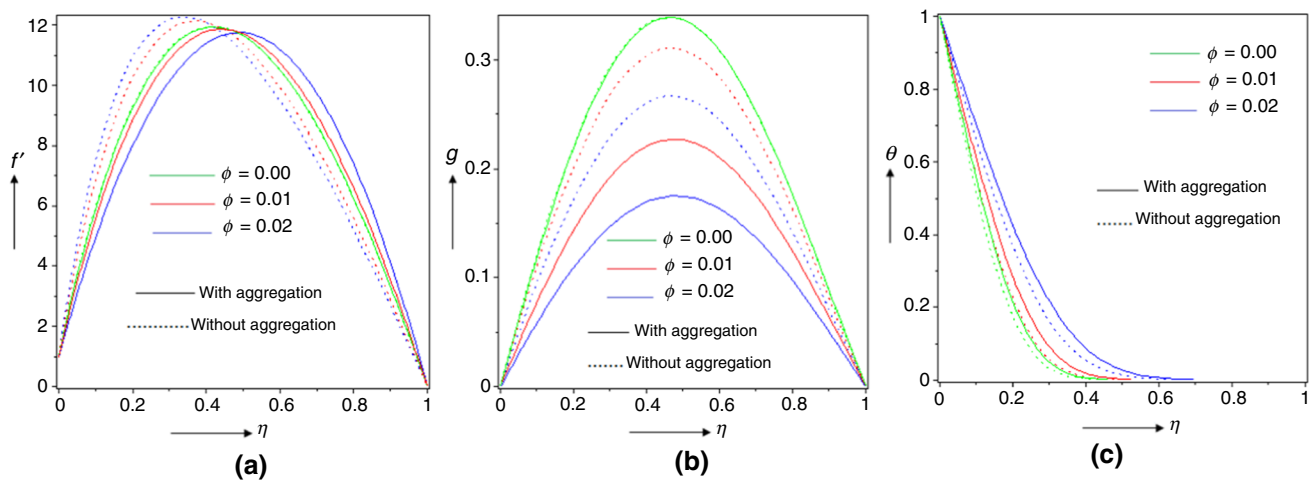

Fig. 12 Effect of ϕ on velocity and temperature

Table 4 it is desirable that surface will be less drag affected for aggregated formation.

Temperature rises for ϕ increasing inside channel. Inside $0.0 \leq \eta \leq 0.8$, effects are undoubtedly clear. In Fig. 12c, comparatively non-aggregated composition illustrates less temperature. Additionally, the addition of nanoparticles holds higher temperature distribution as compared to regular liquid. Nu_r declines at lower segment in both circumstances. But for upper region, Table 5 explores that incorporation of tiny metallic compounds aids heat transfer.

Effect of suction parameter (*S*)

Influence of suction factor on velocity is demonstrated in Fig. 13a, b. Increasing pattern in $f'(\eta)$ is detected for S. Temperature depicts minimum value comparatively for impermeable surface. But when suction amplifies into the surface, high fluctuation in velocity is observed. Non-aggregated composite character of fluid detects comparatively high velocity. It is noteworthy to communicate that for impermeable surface initially velocity slows down inside $0.0 \leq \eta < 0.6$ (*not accurately defined*) and at $\eta = 0.6$ velocity diminishes, but after that velocity again increases. It is exact only for aggregated composite. Initially, peak velocity is attained at the proximity of lower surface, but higher values of S shifts peak value slightly towards the mid-position of the channel. Exactly same scenario is noticed for $g(\eta)$. Velocity again increases for S. Here the velocity graph for suction values is symmetric about mid-position. Hence maximum value is attained at mid-position except $S = 0.0$. Frictional effect in Table 4 seems to ascend at lower part, but at upper region it drops off.

Temperature in Fig. 13c describes reducing aspect for $\phi = 0.02$. It can be determined that increasing values of S

resist the temperature distribution, and hence, it gives the decrease in the temperature. Aggregated property explores high profile. Outcome is prominent inside the entire regime. Heat transfer swells for both situations in Table 5 at lower portion. But upper surface depicts contradict scenario. Figure 14a, b illustrates variation in stream lines for S.

Final remarks

In this literature, impact of aggregation kinetics on the flow of magnetite alloy nanoparticles between two revolving plates has been scrutinized. Upper portion is considered as permeable, while lower portion is stretchable. Nimonic 80A alloy nanoparticles in composition with water as a base solution have been incorporated. Leading equations have been framed via aggregation approach and then solved using RK-4 scheme in conjunction with shooting procedure. Consequences of aggregation factors and flow factors have been deliberated through graphs and tables. Based on entire enquiry, key features are as follows:

- Dual features in $f'(\eta)$ are detected for $d_f, d_l, \phi, R, \delta$, but ups and down in profile are confirmed for λ.
- Most importantly, velocity $f'(\eta)$ reduces for aggregation due to nanoparticle concentration, whereas the absence of aggregation provides opposite syndrome.
- Velocity along z-direction, i.e. $g(\eta)$, reduces for S, ϕ while rest of the factors explores the opposite.
- Temperature depicts decaying scenario for d_f, δ, S, but enhances for d_l, ϕ, R, λ.
- Effective thermal conductivity drops off due to A_k, but enhances for ϕ.
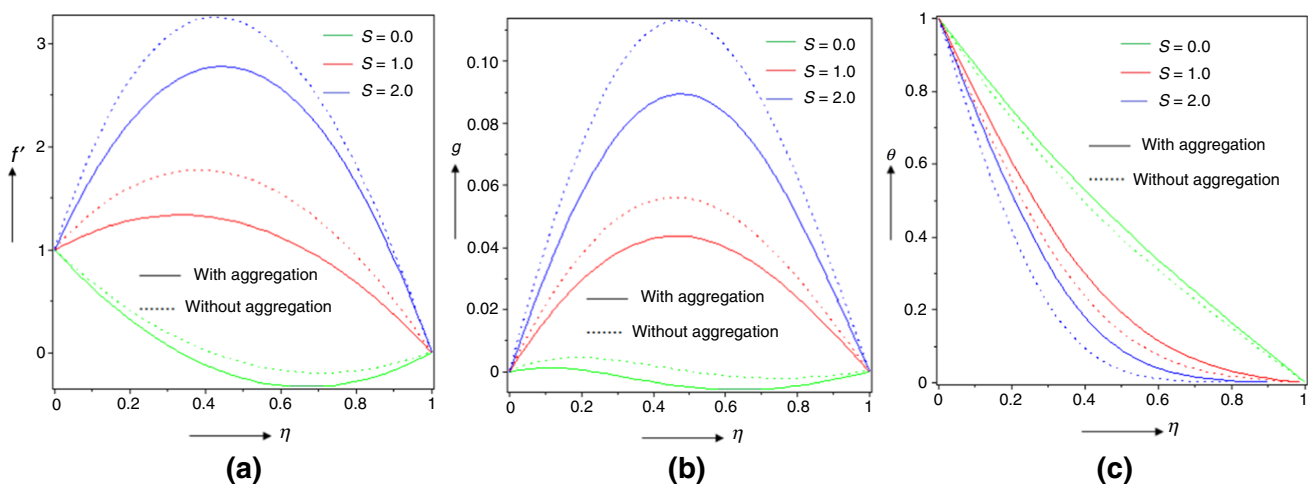- Aggregated factors aid frictional symptom to enhance at both surfaces.

Fig. 13 Effect of S on velocity and temperature
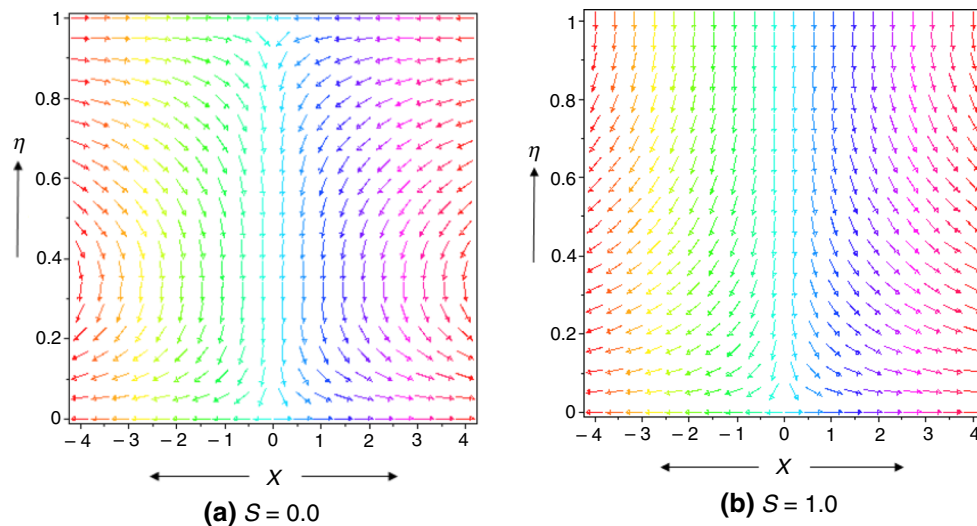
(a) $S = 0.0$

(b) $S = 1.0$

Fig. 14 Effect of S on stream lines

- Particle volume fraction provides increasing features for C_{fr} at lower regime in the absence of aggregation, but generates reverse scenario for aggregated composite.
- Lower surface experiences reduction in Nu_r due to d_1, R but opposite characteristic was carried out for upper portion. Additionally d_f promotes heat transport at lower segment.
- Upper section explores elevated heat transport features for ϕ, λ, but reverse is preserved at lower part. More importantly, situation completely switches over for δ, S.

References

1. Choi SUS. Enhancing thermal conductivity of fluids with nanoparticles. Dev Appl Non-Newton Flows. 1995;66:99–105.
2. Eastman JA, Choi US, Li S, Thompson LJ, Lee S. Enhanced thermal conductivity through the development of nanofluids. In: Komarneni S, Parker JC, Wollenberger HJ, editors. Nanophase and nanocomposite materials II. Pittsburg: MRS; 1997. p. 3–11.
3. Bozorgan N, Shafahi M. Performance evaluation of nanofluids in solar energy: a review of the recent literature. Micro Nano Syst Lett. 2015;3:5. https://doi.org/10.1186/s40486-015-0014-2.
4. Yang L, Hu Y. Toward TiO$_2$ nanofluids—Part 2: applications and challenges. Nanoscale Res Lett. 2017;12:446.
5. Li MZ, Jia LC, Zhang XP, Yan DX, Zhang QC, Li Z. M, Robust carbon nanotube foam for efficient electromagnetic interference shielding and microwave absorption. J Colloid Interface Sci. 2018;530(15):113–9.
6. Medrano JJA, Aragon FFH, Felix LL, Coaquira JAH, Rodriguez AFR, Faria FSEDV, Sousa MH, Ochoa JCM, Morais PC. Evidence of particle–particle interaction quenching in nanocomposite based on oleic acid-coated Fe$_3$O$_4$ nanoparticles after overcoating with essential oil extracted from *Croton cajucara Benth*. JMagn Magn Mater. 2018;466(15):359–67.
7. Manimaran R, Palaniradja K, Alagumurthi N, Sendhilnathan S, Hussain J. Preparation and characterization of copper oxide nanofluid for heat transfer applications. Appl Nanosci. 2014;4(2):163–7.
8. Acharya N, Das K, Kundu PK. Framing the effects of solar radiation on magneto-hydrodynamics bioconvection nanofluid flow in presence of gyrotactic microorganisms. J Mol Liq. 2016;222:28–37.
9. Akbar NS, Beg OA, Khan ZH. Magneto-nanofluid flow with heat transfer past a stretching surface for the new heat flux model using numerical approach. Int J Numer Meth Heat Fluid Flow. 2017;27(6):1215–30.
10. Ismael MA, Mansour MA, Chamkha AJ, Rashad A. M, Mixed convection in a nanofluid filled-cavity with partial slip subjected to constant heat flux and inclined magnetic field. J Magn Magn Mater. 2016;416:25–36.
11. Ghadikolaei SS, Hosseinzadeh Kh, Ganji D. D, MHD raviative boundary layer analysis of micropolar dusty fluid with graphene oxide (Go)- engine oil nanoparticles in a porous medium over a stretching sheet with joule heating effect. Powder Technol. 2018;338:425–37.
12. Mahian O, Kolsi L, Amani M, et al. Recent advances in modeling and simulation of nanofluid flows-part I: fundamental and theory. Phys Rep. 2018. https://doi.org/10.1016/j.physrep.2018.11.004.
13. Mahian O, Kolsi L, Amani M, et al. Recent advances in modeling and simulation of nanofluid flows-part II: applications. Phys Rep. 2018;10:12. https://doi.org/10.1016/j.physrep.2018.11.003.
14. Yousefi T, Veysi F, Shojaeizadeh E, Zinadini S. An experimental investigation on the effect of Al$_2$O$_3$–H$_2$O nanofluid on the efficiency of flat plate solar collector. Renew Energy. 2012;39(1):293–8.
15. Gangadevi R, Vinayagam BK. Experimental determination of thermal conductivity and viscosity of different nanofluids and its effect on a hybrid solar collector. J Therm Anal Calorim. 2018. https://doi.org/10.1007/s10973-018-7840-4.
16. Annapureddy HVR, Nune SK, Motkuri RK, McGrail BP, Dang LX. A combined experimental and computational study on the stability of nanofluids containing metal organic frameworks. J Phys Chem B. 2015;119(29):8992–9.
17. Wang Y, Deng KH, Liu B, Wu JM, Su GH. Experimental study on AlN/H$_2$O and Al$_2$O$_3$/H$_2$O nanofluid flow boiling heat transfer and its influence factors in a vertical tube. In: ASME Proceedings

thermal-hydraulics, Paper No. ICONE24-60496. https://doi.org/10.1115/icone24-60496.

18. Bowers J, Cao H, Qiao G, Li Q, Zhang G, Mura E, Ding Y. Flow and heat transfer behaviour of nanofluids in microchannels. Prog Nat Sci: Mater Int. 2018;28(2):225–34.

19. Peyravi A, Keshavarz P, Mowla D. Experimental investigation on the absorption enhancement of CO_2 by various nanofluids in hollow fiber membrane contactors. Energy Fuels. 2015;29(12):8135–42.

20. Adelekan DS, Ohunakin OS, Gill J, Atayero AA, Diarra CD, Asuzu EA. Experimental performance of a safe charge of LPG refrigerant enhanced with varying concentrations of TiO_2 nano-lubricants in a domestic refrigerator. J Therm Anal Calorim. 2018. https://doi.org/10.1007/s10973-018-7879-2.

21. Teng TP, Hung YH, Teng TC, Chen JH. Performance evaluation on an air-cooled heat exchanger for alumina nanofluid under laminar flow. Nanoscale Res Lett. 2011;6:488. https://doi.org/10.1186/1556-276X-6-488.

22. Moghaddaszadeh N, Esfahani JA, Mahian O. Performance enhancement of heat exchangers using eccentric tape inserts and nanofluids. J Therm Anal Calorim. 2019. https://doi.org/10.1007/s10973-019-08009-x.

23. Freidoonimehr N, Rostami B, Rashidi MM, Momoniat E. Analytical modelling of three-dimensional squeezing nanofluid flow in a rotating channel on a lower stretching porous wall. Math Probl Eng. 2014;692–728.

24. Mohyud-Din ST, Zaidi ZA, Khan U, Ahmed N. On heat and mass transfer analysis for the flow of a nanofluid between rotating parallel plates. Aerosp Sci Technol. 2015;46:514–22.

25. Sheikholeslami M, Hatami M, Ganji DD. Nanofluid flow and heat transfer in a rotating system in the presence of a magnetic field. J Mol Liq. 2014;190:112–20.

26. Mabood F, Khan WA, Makinde OD. Hydromagnetic flow of a variable viscosity nanofluid in a rotating permeable channel with hall effects. J Eng Thermophys. 2017;26:553–66.

27. Hayat T, Qayyum S, Imtiaz M, Alzahrani F, Alsaedi A. Partial slip effect in flow of magnetite Fe_3O_4 nanoparticles between rotating stretchable disks. J Magn Magn Mater. 2016;413:39–48.

28. Mustafa M. MHD nanofluid flow over a rotating disk with partial slip effects: Buongiorno model. Int J Heat Mass Transf. 2017;108:1910–6.

29. Acharya N, Das K, Kundu PK. Fabrication of active and passive controls of nanoparticles of unsteady nanofluid flow from a spinning body using HPM. Eur Phys J Plus. 2017;132:323.

30. Acharya N, Das K, Kundu PK. Rotating flow of carbon nanotube over a stretching surface in the presence of magnetic field: a comparative study. Appl Nanosci. 2018. https://doi.org/10.1007/s13204-018-0794-9.

31. Hogan CCM. Density of states of an insulating ferromagnetic alloy. Phys Rev. 1969;188:870.

32. Parayanthal P, Pollak F. Raman scattering in alloy semiconductors:" spatial correlation" model. Phys Rev Lett. 1984;52:1822–5.

33. Smith RJ, Lewi GJ, Yates DH. Development and application of nickel alloys in aerospace engineering. Aircr Eng Aerosp Technol. 2001;73(2):138–47. https://doi.org/10.1108/00022660110694995.

34. Heckman GR, Herbenar AW. Operating experience of Nimonic 80A first stage buckets in natural gas burning turbines. In: ASME proceedings gas turbine power, Paper No. 60-GTP-8. 1960. https://doi.org/10.1115/60-gtp-8.

35. Kargarnejad S, Djavanroodi F. Failure assessment of Nimonic 80A gas turbine blade. Eng Fail Anal. 2012;26:211–9.

36. Kim DK, Kim DY, Ryu SH, Kim DJ. Application of nimonic 80A to the hot forging of an exhaust valve head. J Mater Process

37. Technol. 2001;113(1):148–52. https://doi.org/10.1016/S0924-0136(01)00700-2.

37. Yerrennagoudaru H, Manjunatha K. Design and development of a new pistonusing Nimonic alloy 80A for low cetane fuels usage in CI engines. Mater Today Proc. 2017;4(8):9284–93.

38. Jeong HS, Cho JR, Lee NK, Park HC. Simulation of electric upsetting and forging process for large marine diesel engine exhaust valves. Mater Sci Forum. 2006;510–511(2006):142–5. https://doi.org/10.4028/www.scientific.net/MSF.510-511.142.

39. Raju CSK, Hoque MM, Anika NN, Mamatha SU, Sharma P. Natural convective heat transfer analysis of MHD unsteady car-reau nanofluid over a cone packed with alloy nanoparticles. Powder Technol. 2017;10:12. https://doi.org/10.1016/j.powtec.2017.05.003.

40. Makinde OD, Mahanthesh B, Gireesha BJ, Shashikumar NS, Monaledi RL, Tshehla MS. MHD nanofluid flow past a rotating disk with thermal radiation in the presence of aluminum and titanium alloy nanoparticles. Defect Diffusion Forum. 2018;384:69–79.

41. Sandeep N, Sugunamma V, Krishna PM. Effects of radiation on an unsteady natural convective flow of a EG-Nimonic 80a nanofluid past an infinite vertical plate. Adv Phys Theor Appl. 2013;23:36–43.

42. Sandeep N, Sulochana C, Sugunamma V. Heat transfer characteristics of a dusty nanofluid past a permeable stretching/shrinking cylinder with non-uniform heat source/sink. J Nanofluids. 2016;5:59–67.

43. Ellahi R, Hassan M, Zeeshan A, Khan AA. The shape effects of nanoparticles suspended in HFE-7100 over wedge with entropy generation and mixed convection. Appl Nanosci. 2016;6:641–51.

44. Keblinski P, Phillpot SR, Choi SUS, et al. Mechanisms of heat flow in suspensions of nano-sized particles (nanofluids). Int J Heat Mass Transf. 2002;45:855–63.

45. Wang BX, Zhou LP, Peng XF. A fractal model for predicting the effective thermal conductivity of liquid with suspension of nanoparticles. Int J Heat Mass Transf. 2003;46:2665–72.

46. Prasher R, Phelan PE, Bhattacharya P. Effect of aggregation kinetics on the thermal conductivity of nanoscale colloidal solutions (nanofluid). Nano Lett. 2006;6:1529–34.

47. Evans W, Prasher R, Fish J, Meakin P, Phelan P, Keblinski P. Effect of aggregation and interfacial thermal resistance on thermal conductivity of nanocomposites and colloidal nanofluids. Int. J. Heat Mass Transf. 2008;51:1431–8.

48. Sui J, Zhao P, Mohsin BB, Zheng L, Zhang X, Cheng Z, Chen Y, Chen G. Fractal aggregation kinetics contributions to thermal conductivity of nano-suspensions in unsteady thermal convection. Sci Rep. https://doi.org/10.1038/srep39446.

49. Gambinossi F, Mylon SE, Ferri JK. Aggregation kinetics and colloidal stability of functionalized nanoparticles. Adv Colloid Interface Sci. https://doi.org/10.1016/j.cis.2014.07.015.

50. Cai J, Hu X, Xiao B, Zhou Y, Wei W. Recent developments on fractal-based approaches to nanofluids and nanoparticle aggregation. Int J Heat Mass Transf. 2017;105:623–37.

51. Afrooz ARMN, Hussain SM, Saleh NB. Aggregate size and structure determination of nanomaterials in physiological media: importance of dynamic evolution. J Nanopart Res. 2014;16:1–7.

52. Prasher RS, Bhattacharya P, Phelan PE. Brownian motion based convective conductive model for the effective thermal conductivity of nanofluids. J Heat Transf. 2006;128:588–95.

53. Jang SP, Choi SUS. Role of Brownian motion in the enhanced thermal conductivity of nanofluids. Appl Phys Lett. 2004;84:4316–8.

54. Keblinski P, Eastman JA, Cahill DG. Review feature nanofluid for thermal transport. Mater Today. 2005;8:36–44.

55. Hunter RJ. Foundations of colloid science. New York: Oxford University Press; 2001.

56. Zhu H, Zhang C, Liu S, Tang Y, Yin Y. Appl Phys Lett. 2006;89:023123.
57. Ce-Wen Nan R, Birringer R, Clarke DR, Gleiter H. Effective thermal conductivity of particulate composites with interfacial thermal resistance. J Appl Phys. 1997;81(10):6692–9.
58. Venerus DC, Kabadi MS, Lee S, Perez-Luna V. Study of thermal transport in nanoparticle suspensions using forced Rayleigh scattering. J Appl Phys. 2006;100:094310–1–094310-2.
59. Shih W-H, Shih WY, Kim S-I, Liu J, Aksay IA. Scaling behavior of the elastic properties of colloidal gels. Phys Rev A. 1990;42:4772–9.
60. Prasher RS. Thermal interface materials: historical perspective, status, and future directions. Proc IEEE. 2006;94(8):1571–86.
61. Putnam SA, Cahill DG, Ash BJ, Schadler LS. High-precision thermal conductivity measurements as a probe of polymer/nanoparticles interfaces. J Appl Phys. 2003;94(10):6785–8.